12th International Symposium on Turbulence and Shear Flow Phenomena (TSFP12)
Osaka, Japan, July 19–22, 2022

FLOW PAST SUDDEN STEP-CHANGE IN SURFACE TOPOGRAPHY FROM STREAMWISE RIDGES TO SMOOTH WALL

Takfarinas Medjnoun
Aerodynamics and Flight Mechanics
University of Southampton
Southampton SO16 7QF, UK
t.medjnoun@soton.ac.uk

Bharathram Ganapathisubramani
Aerodynamics and Flight Mechanics
University of Southampton
Southampton SO16 7QF, UK
g.bharath@soton.ac.uk

INTRODUCTION

Within the last two decades, the recent advances in wall-bounded turbulence have considerably extended our understanding of rough-wall flow physics (Chung *et al.*, 2021), but have additionally shed more light on the challenges in predicting the drag, essentially, due to the complex nature of the rough-wall and turbulent flow interactions. *A fortiori*, predicting drag becomes even harder when considering spanwise heterogeneous rough-wall surfaces (Medjnoun *et al.*, 2018). These surfaces have come under scrutiny to investigate the mechanisms behind the manifestation of the resulting large-scale secondary motions/currents, which entail a highly three-dimensional flow with alternating high- and low-momentum pathways (Mejia-Alvarez & Christensen, 2013). These have now been fairly-well explored across a wide range of surface conditions such as in rough-wall channels (Willingham *et al.*, 2014; Anderson *et al.*, 2015; Chung *et al.*, 2018; Castro *et al.*, 2021; Schäfer *et al.*, 2022), open-channels and river flows (Nezu *et al.*, 1993; Wang & Cheng, 2006; Zampiron *et al.*, 2021), pipes and Taylor-Couette flows (Chan *et al.*, 2018; Bakhuis *et al.*, 2020) but also in boundary layers (Nugroho *et al.*, 2013; Barros & Christensen, 2014; Medjnoun *et al.*, 2020; Wangsawijaya *et al.*, 2020; Xu *et al.*, 2020). The emergence of these secondary flows is shown to be tied to the spanwise characteristic wavelength of the surface but can also be influenced by other factors such as; the geometry, the amplitude, directionality and perhaps above all, the type of heterogeneity; ridge-type, strip-type or mixed-heterogeneity (Medjnoun *et al.*, 2020, 2021). In addition to the large-scale modification in the mean and turbulent flow structures, recent studies have shown these secondary flows can substantially affect the heat transfer properties of the flow (Stroh *et al.*, 2020; Bon & Meyers, 2022).

Despite the current vast body of work on secondary flows, the development of these structures past a heterogeneous-to-homogeneous step-change remains unexplored. In fact, to our knowledge, all of the existing literature on step-changes exclusively consider flows growing over homogeneous surfaces undergoing either smooth-to-rough or rough-to-smooth changes (Antonia & Luxton, 1971, 1972). These studies have shown that when a turbulent boundary layer experiences roughness discontinuities, a new internal layer begins growing farther downstream (Garratt, 1990). While within the old "outer" layer the mean and turbulent flow remains characteristic of the upstream boundary condition, an equilibrium layer grows which adjusts to the new surface condition (Hanson & Ganapathisubramani, 2016). On the other hand, turbulent boundary layers with secondary flows are shown to reach a self-preserved form after a given distance downstream, with only a weak growth rate (Hwang & Lee, 2018). This observation leads to the main question: to what extent secondary flows can persist past a heterogeneous-to-homogeneous step-change? To examine this question, we specifically designed an experimental study to investigate the streamwise development of these large-scale secondary motions along with their impact on the frictional drag. The consequences on the internal boundary layer, turbulent properties as well as the validity of the classical scaling laws will further be discussed.

EXPERIMENTAL METHODS

Surface heterogeneity

The measurement campaign has been performed in an open-circuit suction wind tunnel at the University of Southampton (see Medjnoun *et al.* (2020) for details). The surface heterogeneity was modelled using a smooth ridge of a rectangular shape, made of clear perspex. These ridges extended from the test section inlet over a length of 40δ (δ being the spanwise-averaged boundary layer thickness measured 2.8m downstream the inlet), before we imposed a step-change to a smooth wall, where we define the streamwise origin (see figure 1). The nominal heights and spanwise spacings were h = 6 mm and S = 80 mm, chosen to match 0.1 and 1 times δ, respectively, to maximize potential secondary flows.

Oil-film interferometry

The frictional drag is directly measured through the interferometry technique. Oil droplets with widths less than 0.1δ (to obtain spanwise-independent measures) are deposited at various spanwise locations. The droplets are then illuminated using a sodium lamp with a wavelength of 589 nm. A 16 MP camera with a 200 mm lens set at an angle of 25^o from the vertical is used and fitted to a Scheimpflug adapter to satisfy the Scheimpflug condition. A calibration target positioned at the wall in the (x,z)-plane is used to calibrate the camera, resulting in a FOV of around $0.6S \times 1.2S$ in the (x,z)-plane, allowing a simultaneous capture of the development of different spanwise interferograms. 100 images per streamwise location at a nominal speed of $U_\infty = 20$ m/s are acquired for 10 minutes in any given run. This process is repeated several times at various streamwise locations to cover the variation of the skin friction in the non-equilibrium region, and reconstruct a map of the skin friction with an extent of $8S \times 1.2S$ in the (x,z)-plane.

Particle image velocimetry

The flow is diagnosed in the cross-plane (y,z) using stereoscopic PIV measurements at four different streamwise stations. The flow is traced by vaporised glycerol-water particles, then illuminated with a laser light sheet sourced by a two-pulse laser operating at 250 mJ. An optical system for the beam focus/expansion of the light sheet is used to obtain a constant thickness in the measurement plane. The particle images are recorded by 16 MP cameras fitted with 200 mm lenses and mounted on Scheimpflug adapters to account for the oblique view angle ($\pm 42^o$). A double-sided dual-plane calibration target aligned with the laser light sheet is used to determine the mapping function for each setup, using a third-order polynomial fit. This resulted in a FOV of $2\delta \times 3\delta$ in the (y,z)-plane. 3000 statistically independent realizations of image pairs are acquired for each case at 0.6 Hz, with a time delay between pulses of 20 μs, at a free-stream velocity U_∞ of 20 m/s. The velocity vector fields are subsequently obtained by interrogating particle images using a decreasing multipass scheme starting from 48 pixels × 48 pixels to a final pass of 24 pixels × 24 pixels with 50% overlap, resulting in an effective vector spacing of 0.55 mm.

RESULTS

Frictional drag

Figure 2 illustrates the response of the oil-droplet interferograms to the surface shear stress caused by both the streamwise and spanwise topographical changes. Although the magnitudes remain less evident to observe, clear directional modifications are depicted as well as a presence of a recirculation region past the streamwise step. This region herein labelled R1, is believed to be home to a highly unsteady flow caused by the separation of the shear layer above and on the side ridges (marked in blue). As the flow reaches the streamwise step-change, these streaks deviate from the streamwise alignment and end up in the recirculation past the ridge. The streamwise extent of the separation is estimated to be within 2-3h. Between the spanwise peak and valley symmetry planes a "buffer" region named R2 highlighted in red, is shown to be affected by the streamwise step as the streaks diverge and expand away from the centre plane. Past the reattachment point (marked with a dark-white dashed line) they are observed to slightly revert back showing a more parallel trajectory with respect to the flow direction. Further away from the ridges, the streaks labelled R3 (marked in black) remain parallel to the flow with a very weak expansion. However at the valley symmetry plane ($z/S = 0$), the streaks remain insensitive to the presence of a step-change.

The quantifications of the changes in the wall shear stress are presented in figure 3, showing the variations caused by the spanwise topographical variation at different streamwise locations. The spanwise distribution of the friction velocity (U_τ) is illustrated in figure 3(a) and is shown to vary periodically with weak (negative for $x < 3h$) magnitudes being recorded past the ridge and their vicinities while the valley remains relatively constant across the span. The streamwise development is captured by the colour tone and varies from darkest near the step to lightest farther away, with an overall magnitude of U_τ at the valley symmetry plane being relatively unchanged. This indicates that this part of the flow remains resilient to the presence of a streamwise step-change, as opposed to the flow past the ridge.

The changes between the spanwise peak and valley symmetry planes are further examined and compared with the spanwise-averaged skin-friction coefficient $\langle C_f \rangle$, as seen in figure 3(b). The results show that in the valley, the skin friction remains unaffected by the streamwise step-change and stays constant (within the uncertainty of the measurement) throughout the distance herein explored. However, past the ridge, the skin friction is shown to undergo a sharp increase which is similar to that observed in rough-to-smooth wall step-changes. This is shown to occur for $x < 0.6\delta$ which is followed by a weakening in skin friction between $0.6 < x < 1.5\delta$. Past a certain distance ($x > 1.5\delta$), the skin friction start recovering again with a relatively weak growth rate. The spanwise-averaged friction is illustrated in black and clearly shows the overall skin friction to only marginally grow in the streamwise direction indicating perhaps very minor changes in the near-wall flow behaviour, as opposed to the classical rough-to-smooth flows.

To highlight the difference with the latter flows, two cases from the experimental study of Hanson & Ganapathisubramani (2016) who examined the effect of homogeneous rough-to-smooth transition of a mesh- and grit-type roughness are presented in figure 3(c) The current results indicate that $\langle C_f \rangle$ undergoes strong changes near the step ($x < 0.5\delta$), in contrast with the homogeneous cases which recover slowly. Despite the upstream flow being heterogeneous in the spanwise direction, the near-wall flow shows a faster recovery towards a new "streamwise-equilibrium" state than a homogeneous case. However, this pseudo-equilibrium state (shown by the invariance of the drag) is different from the classical homogeneous rough-to-smooth cases. Considering that large-scale secondary motions have been previously observed in the outer region, the way the outer flow interacts with the near-wall region is likely to be play an important role.

Secondary flows

Combining the oil-film and sPIV measurements, wall-drag as well as flow field information can be presented as in figures 4, which show the normalised mean streamwise velocity (top) and vorticity-signed swirling strength (bottom). The skin friction map is obtained by interpolating nearly three hundred independent (measured) points that covered a surface of $8S \times 1.2S$ in the (x,z)-plane. On the other hand, the cross-plane flow fields are obtained at x/δ=-0.65, 0.2, 4 and 8, respectively. Figure 4 indicated that the flow experienced strong spanwise changes in the form of high- and low-momentum pathways caused by the presence of secondary motions. Their spanwise locations are consistent with those observed in previous studies of topographical heterogeneity (Medjnoun *et al.*, 2020). The figure also shows that despite the presence of a step-change, the outer region remains relatively unaffected whilst developing downstream. As expected, the upstream surface condition caused mean flow heterogeneity illustrated by the high- and low-momentum pathways, themselves associated with high and low friction velocity magnitudes, respectively.

The aforementioned behaviour in the mean flow topology is further substantiated by the identification of secondary motions through the computation of the vorticity-signed swirling strength. The results are shown in the bottom half of figure 4, indicating that secondary motions made of a pair of counter-rotating vortices are located on the top of either side of the ridges, inducing upwash and downwash motions above the ridges and valley, respectively. Right past the step, the contour level of the mean flow map seems to have reduced in the outer region, indicating a relaxation of the overall boundary layer thickness caused by the adverse pressure gradient at the step. Equivalently, a noticeable impact is observed near the wall with a more heterogeneous mean flow. Further downstream, only small changes can be observed from the stations $x/\delta = 4$ and 8 for the outer region, as opposed to the near-wall which seems to recover its previous form.

Besides the main large-scale secondary structures observed, a similar smaller structure constituted of a pair of counter-rotating vortices rotating in opposite direction to the main ones are observed above the ridge. This feature is labelled a tertiary structure in the previous study of Medjnoun *et al.* (2020) which rises due to the geometry of the ridge. This structure is shown to disappear downstream the step, as opposed to the outer region secondary structure which persists further downstream. This observation shows that these large-scale secondary motions are inherently capable of sustaining themselves for longer distances downstream of the step-change, and are capable of maintaining a good degree of self-similarity when encountering homogeneous surfaces. This is in contrast with the tertiary structures which seem incapable of self-sustain without a viscous boundary condition such as the presence of a rectangular ridge, leading to the observed changes in the near-wall region.

Using the triple decomposition method applied to the flow fields in the cross-plane, the dispersive stresses caused by the mean flow heterogeneity can further be examined. For instance, the streamwise velocity field can be expressed as

$$\underbrace{u_i(y,z,t)}_{\substack{\text{Instantaneous}\\ \text{velocity}}} = \overbrace{\underbrace{\langle U(y)\rangle_S}_{\substack{\text{Spatial-time-}\\ \text{averaged}\\ \text{velocity}}} + \underbrace{\tilde{u}(y,z)}_{\substack{\text{Dispersive}\\ \text{velocity}\\ \text{component}}}}^{\text{Time-averaged velocity}} + \underbrace{u(y,z,t)}_{\substack{\text{Random}\\ \text{velocity}\\ \text{component}}}, \qquad (1)$$

where u_i is the instantaneous velocity field measured at a fixed streamwise location. $\langle U(y)\rangle_S$ is the time- and horizontally-averaged velocity profile over the spanwise wavelength S. $\tilde{u}(y,z)$ is the time-invariant spatial deviation field and $u(y,z,t)$ is the time and space dependant fluctuating part from the Reynolds double decomposition. By applying the same method to the different velocity components, the different dispersive stress tensor terms can be evaluated and compared. More specifically, the total shear stress term can be computed as

$$\underbrace{\overline{\tau_{xy}}}_{\substack{\text{total}\\ \text{shear}\\ \text{stress}}} = \underbrace{\nu\frac{\partial U}{\partial y}}_{\substack{\text{viscous}\\ \text{shear}\\ \text{stress}}} - \underbrace{\overline{uv}}_{\substack{\text{turbulent}\\ \text{shear}\\ \text{stress}}} - \underbrace{\overline{\tilde{u}\tilde{v}}}_{\substack{\text{dispersive}\\ \text{shear}\\ \text{stress}}}, \qquad (2)$$

which typically accounts for viscous, turbulent and dispersive shear stress contributions. The viscous contribution is only present very near the wall, which in the current study remains unresolved due to the measurement constraints.

The results are shown in figure 5, presenting comparative maps of the turbulent, dispersive and total shear stresses from left to right, respectively. The maps are shown from upstream of the step-change (top) to the farthest downstream location (bottom). The dispersive stresses are shown to be not negligible with respect to the turbulent ones, extending for nearly two thirds of the boundary layer thickness with varying intensity along the spanwise direction. The magnitude and distribution of the turbulent and dispersive shear stresses differ, with an overall distribution of turbulent stress following the modulation character of the mean flow. On the other hand, the dispersive term is shown to be more localised. Right after the step-change, substantial modifications appear for both the turbulent and dispersive maps. Strong turbulent shear stress events are shown to occur past the ridge, while the turbulence activity in the outer region seems to diffuse vertically and radially, which can be caused by the flow deceleration. This observation hints to a reduction in the overall outer-layer heterogeneity. This is in fact substantiated by the changes that occurred in the dispersive shear stress component, which highlights a reduction in the degree of heterogeneity in the outer region, however with a negative turbulence activity near the wall. This result seems to have also impacted the overall shear stress which shows intense negative turbulence activity past the step. This behaviour is due to strong negative vertical dispersive component past the discontinuity caused by the adjustment of the upstream flow to the new surface condition. Therefore, the reduction of the spanwise heterogeneity comes from a dual effect of the turbulence diffusion due to deceleration as well as the negation between the upstream upwash flow occurring above the ridges and the downwash of the recirculation region imposed by the streamwise step-change. At farther distances downstream the step-change, both turbulent and dispersive shear stresses seem to adopt similar patterns to those observed upstream the step in the outer region. Moreover, the previous observation of a negative dispersive shear stress activity near the wall does not seem to hold for such distances, confirming that it is a consequence of the step-change. The downstream persistence of the dispersive component is in line with the mean flow and swirling strength maps presented before, corroborating the resilience character of these large-scale features. These results suggest that these large-scale secondary flows posses enough inertia to self-sustain for long distances, and can maintain a good degree of self-similarity over a homogeneous surface condition. This also means that in order for these types of turbulent boundary layers to recover spanwise homogeneity, very long distances are required to allow for the diffusion of these secondary motions.

REFERENCES

Anderson, W., Barros, J. M., Christensen, K. T. & Awasthi, A. 2015 Numerical and experimental study of mechanisms responsible for turbulent secondary flows in boundary layer flows over spanwise heterogeneous roughness. *J. Fluid Mech* **768**, 316–347.

Antonia, RA & Luxton, RE 1971 The response of a turbulent boundary layer to a step change in surface roughness part 1. smooth to rough. *J. Fluid Mech* **48** (4), 721–761.

Antonia, RA & Luxton, RE 1972 The response of a turbulent boundary layer to a step change in surface roughness. part

2. rough-to-smooth. *J. Fluid Mech* **53** (4), 737–757.

Bakhuis, D., Ezeta, R., Berghout, P., Bullee, P. A., Tai, D., Chung, D., Verzicco, R., Lohse, D., Huisman, S. G. & Sun, C. 2020 Controlling secondary flow in taylor–couette turbulence through spanwise-varying roughness. *J. Fluid Mech* **883**.

Barros, J. M. & Christensen, K. T. 2014 Observations of turbulent secondary flows in a rough-wall boundary layer. *J. Fluid Mech* **748**.

Bon, T & Meyers, J 2022 Stable channel flow with spanwise heterogeneous surface temperature. *J. Fluid Mech.* **933**.

Castro, I. P., Kim, J. W., Stroh, A. & Lim, H. C. 2021 Channel flow with large longitudinal ribs. *J. Fluid Mech.* **915**.

Chan, L., MacDonald, M., Chung, D., Hutchins, N. & Ooi, A. 2018 Secondary motion in turbulent pipe flow with three-dimensional roughness. *J. Fluid Mech* **854**, 5–33.

Chung, D., Hutchins, N., Schultz, M. P. & Flack, K. A. 2021 Predicting the drag of rough surfaces. *Ann. Rev. Fluid Mech.* **53**, 439–471.

Chung, D., Monty, J. P. & Hutchins, N. 2018 Similarity and structure of wall turbulence with lateral wall shear stress variations. *J. Fluid Mech* **847**, 591–613.

Garratt, J. R. 1990 The internal boundary layer — a review. *Boundary-Layer Met* **50** (1), 171–203.

Hanson, R.ÂE. & Ganapathisubramani, B. 2016 Development of turbulent boundary layers past a step change in wall roughness. *J. Fluid Mech* **795**, 494–523.

Hwang, H. G. & Lee, J. H. 2018 Secondary flows in turbulent boundary layers over longitudinal surface roughness. *Phys. Rev. Fluids* **3**, 014608.

Medjnoun, T., Rodriguez-Lopez, E., Ferreira, M. A., Griffiths, T., Meyers, J. & Ganapathisubramani, B. 2021 Turbulent boundary-layer flow over regular multiscale roughness. *J. Fluid Mech.* **917**.

Medjnoun, T., Vanderwel, C. & Ganapathisubramani, B. 2018 Characteristics of turbulent boundary layers over smooth surfaces with spanwise heterogeneities. *J. Fluid Mech* **838**, 516–543.

Medjnoun, T., Vanderwel, C. & Ganapathisubramani, B. 2020 Effects of heterogeneous surface geometry on secondary flows in turbulent boundary layers. *J. Fluid Mech* **886**.

Mejia-Alvarez, R. & Christensen, K. T. 2013 Wall-parallel stereo particle-image velocimetry measurements in the roughness sublayer of turbulent flow overlying highly irregular roughness. *Phys. Fluids* **25** (11), 115109.

Nezu, I., Tominaga, A. & Nakagawa, H. 1993 Field measurements of secondary currents in straight rivers. *J. Fluids Eng.* **119** (5), 598–614.

Nugroho, B., Hutchins, N. & Monty, J. P. 2013 Large-scale spanwise periodicity in a turbulent boundary layer induced by highly ordered and directional surface roughness. *Intl J. Heat Fluid Flow* **41**, 90–102.

Schäfer, K, Stroh, A, Forooghi, P & Frohnapfel, B 2022 Modelling spanwise heterogeneous roughness through a parametric forcing approach. *J. Fluid Mech.* **930**.

Stroh, A, Schäfer, K, Forooghi, P & Frohnapfel, B 2020 Secondary flow and heat transfer in turbulent flow over streamwise ridges. *International Journal of Heat and Fluid Flow* **81**, 108518.

Wang, Z. Q. & Cheng, N. S. 2006 Time-mean structure of secondary flows in open channel with longitudinal bedforms. *Adv. Water Resour* **29** (11), 1634–1649.

Wangsawijaya, D. D., Baidya, R., Chung, D., Marusic, I. & Hutchins, N. 2020 The effect of spanwise wavelength of surface heterogeneity on turbulent secondary flows. *J. Fluid Mech* **894**.

Willingham, D., Anderson, W., Christensen, K. T. & Barros, J. M. 2014 Turbulent boundary layer flow over transverse aerodynamic roughness transitions: induced mixing and flow characterization. *Phys. Fluids* **26** (2), 025111.

Xu, F., Zhong, S. & Zhang, S. 2020 Experimental study on secondary flow in turbulent boundary layer over spanwise heterogeneous microgrooves. *Phys Fluids.* **32** (3), 035109.

Zampiron, A., Cameron, S. & Nikora, V. 2021 Momentum and energy transfer in open-channel flow over streamwise ridges. *J. Fluid Mech* **915**.

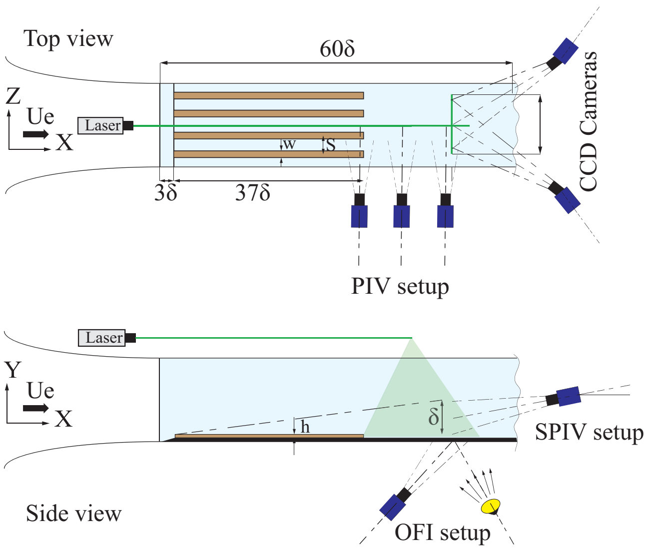

Figure 1: Schematics of the experimental arrangement of the surface step-change including the Planar/Stereo PIV setup (top) and the Oil-film interferometry setups (bottom).

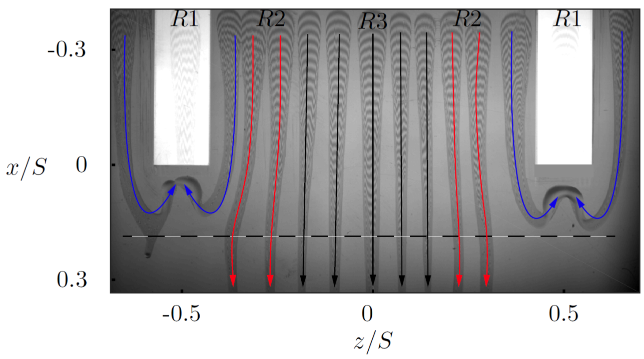

Figure 2: Example of oil droplets deposited upstream the step-change at U_∞ = 20 m/s with streamlines drawn to highlight the pattern displayed by the OFI streaks.

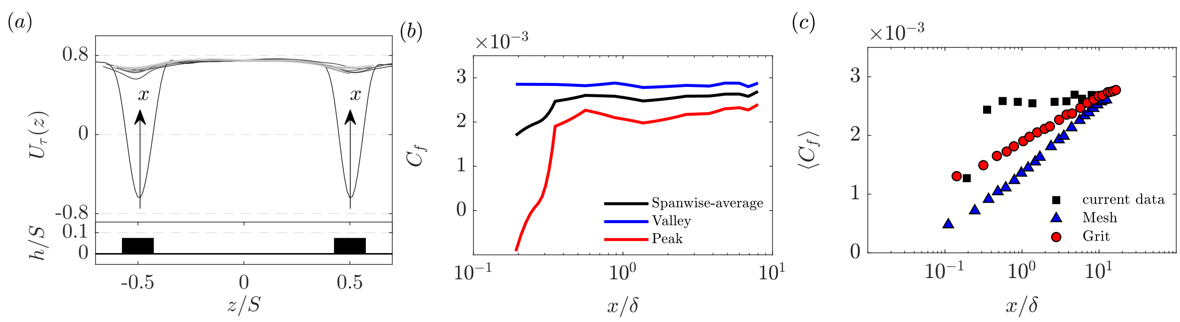

Figure 3: (a) Spanwise variation of the friction velocity across different streamwise stations highlighted in dark (near the step) to light grey (farther). (b) Comparison of the spanwise-averaged, peak and valley skin-friction coefficient, as a function of the streamwise distance normalised by the upstream boundary layer thickness δ. (b) Comparison of the spanwise-averaged friction coefficient with the rough-to-smooth step-change cases from Hanson & Ganapathisubramani (2016).

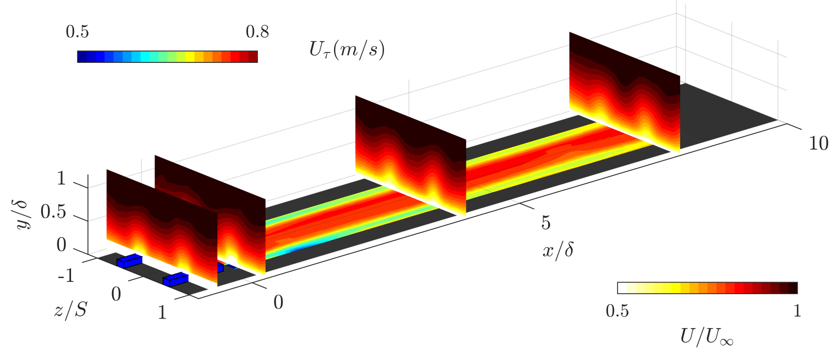

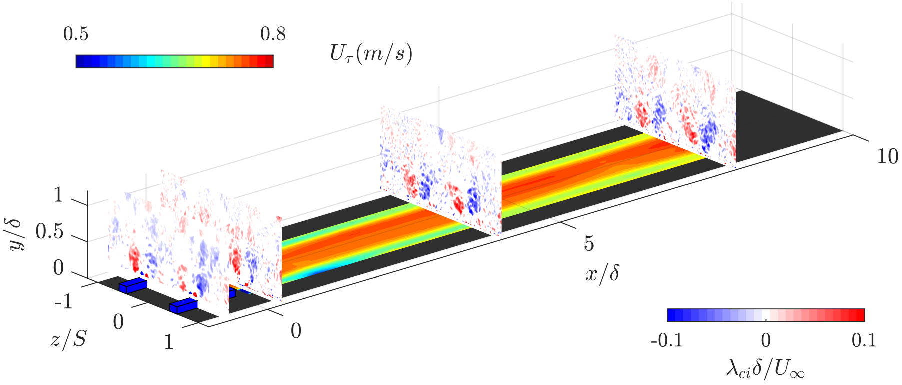

Figure 4: Cross-plane of the (top) normalized mean streamwise velocity and (bottom) vorticity-signed swirling strength at different streamwise locations along the friction velocity map.

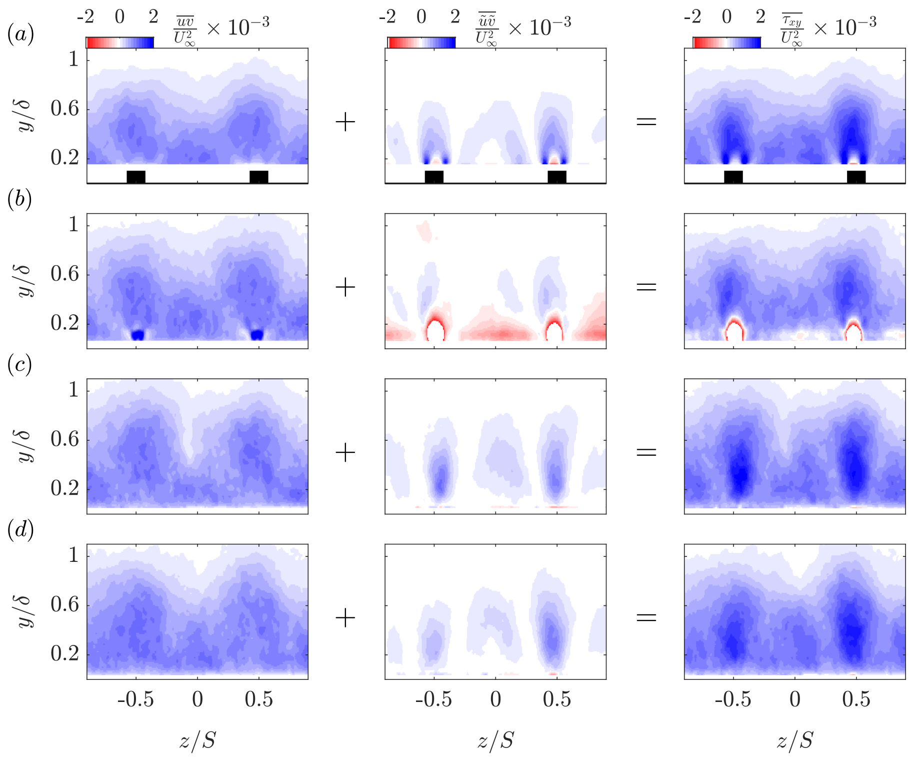

Figure 5: Contour maps of the normalised turbulent (left), dispersive (middle) and total (right) shear stress for the different streamwise locations, going from top (upstream the step-change) to bottom (furthest location).